



Article

Meso-Neoproterozoic Mafic Sills along the South-Eastern Margin of the Siberian Craton, SE Yakutia: Petrogenesis, Tectonic and Geochemical Features

Aleksandr D. Savelev ^{1,2,*} , Sergey V. Malyshev ² , Valery M. Savatenkov ^{2,3},
Daniil D. Ignatov ² and Anastasia D. Kuzkina ²

¹ Faculty of Geology and Geography, Tomsk State University, 634050 Tomsk, Russia

² Institute of Earth Sciences, St. Petersburg State University, 199034 St. Petersburg, Russia; s.malyshev@spbu.ru (S.V.M.); v.m.savatenkov@ipgg.ru (V.M.S.); ignatovdd@gmail.com (D.D.I.); anastasia.d.kuzkina@gmail.com (A.D.K.)

³ Institute of Precambrian Geology and Geochronology, Russian Academy of Sciences, 199034 St. Petersburg, Russia

* Correspondence: aleksandr.d.savelev@gmail.com; Tel.: +7-921-796-4959

Received: 10 August 2020; Accepted: 10 September 2020; Published: 12 September 2020



Abstract: We report major and trace element concentrations, along with Nd isotope compositions, for Late Mesoproterozoic to Early Neoproterozoic dolerite sills from the Sette-Daban ridge (southern Verkhoyansk, south-east Siberia). Based on their major element composition, all rocks correspond to low-Ti (<3 wt% TiO₂) moderately alkaline basalts. The intrusions can be subdivided into two groups based on their trace element compositions. One group includes sills mainly distributed in the southern part of the study area (Yudoma group), with mid-ocean ridge basalt (MORB) trace element patterns enriched in aqueous fluid mobile incompatible (FMI) elements (Sr, Pb, Ba, U). The second group includes sills mostly distributed in the northern part of the study area, enriched in immobile incompatible (II) elements (Th, Nb, light rare earth elements (LREE)) and to a lesser extent, in aqueous fluid mobile elements. The Nd isotope signatures of the dolerites characterize a depleted mantle source, with a small enrichment from recycled continental crust. The geochemical characteristics of these igneous rocks are analogous to low-Ti basalts of large intraplate provinces (e.g., the Karoo and Siberian Traps). We propose that they formed by rifting-induced melting of the heterogeneous metasomatized shallow spinel-bearing mantle zone. We suggest that two different melting sources were involved in the generation of the two geochemically distinct sill groups, including the addition of two different subduction components. The southern sills were formed by melting of depleted lithospheric mantle enriched with FMI elements, corresponding to subduction-induced metasomatic alteration by fluids at shallow depths. The northern dolerites were formed by melting of depleted lithospheric mantle enriched with II elements, associated with the melting of subducted sediments at deeper depths.

Keywords: South-East Siberia; Sette-Daban; mafic rock; sills; geochemistry; metasomatized mantle

1. Introduction

The sedimentary succession deposited along the south-eastern margin of the Siberian Craton (Figure 1) includes carbonate and clastic rocks ranging in age from Mesoproterozoic to Mesozoic, and records the long-term evolution from an intracratonic basin to a passive margin, and finally to a fold-and-thrust belt [1–4]. Several mafic magmatic events accompanied the pre-Mesozoic evolution

of the eastern Siberian Craton margin, including Mesoproterozoic, latest Mesoproterozoic to early Neoproterozoic, early Paleozoic, and Devonian events [5–7]. Paleozoic mafic magmatic events have been described and discussed in many papers, and are mainly reported from the eastern margin of the Siberian Craton [2,5,6,8,9]. The latest Mesoproterozoic to early Neoproterozoic mafic magmatic event, commonly known as the Sette-Daban event [8], was dated by U-Pb baddeleyite and Sm-Nd isochron methods [6,10,11], but very limited information has been published on the geochemical and isotopic compositions of the associated igneous rocks [6,9]. The main goal of this study is to present new data on the geochemical and isotopic compositions of the latest Mesoproterozoic to early Neoproterozoic mafic intrusions and shed new light on their tectonic setting.

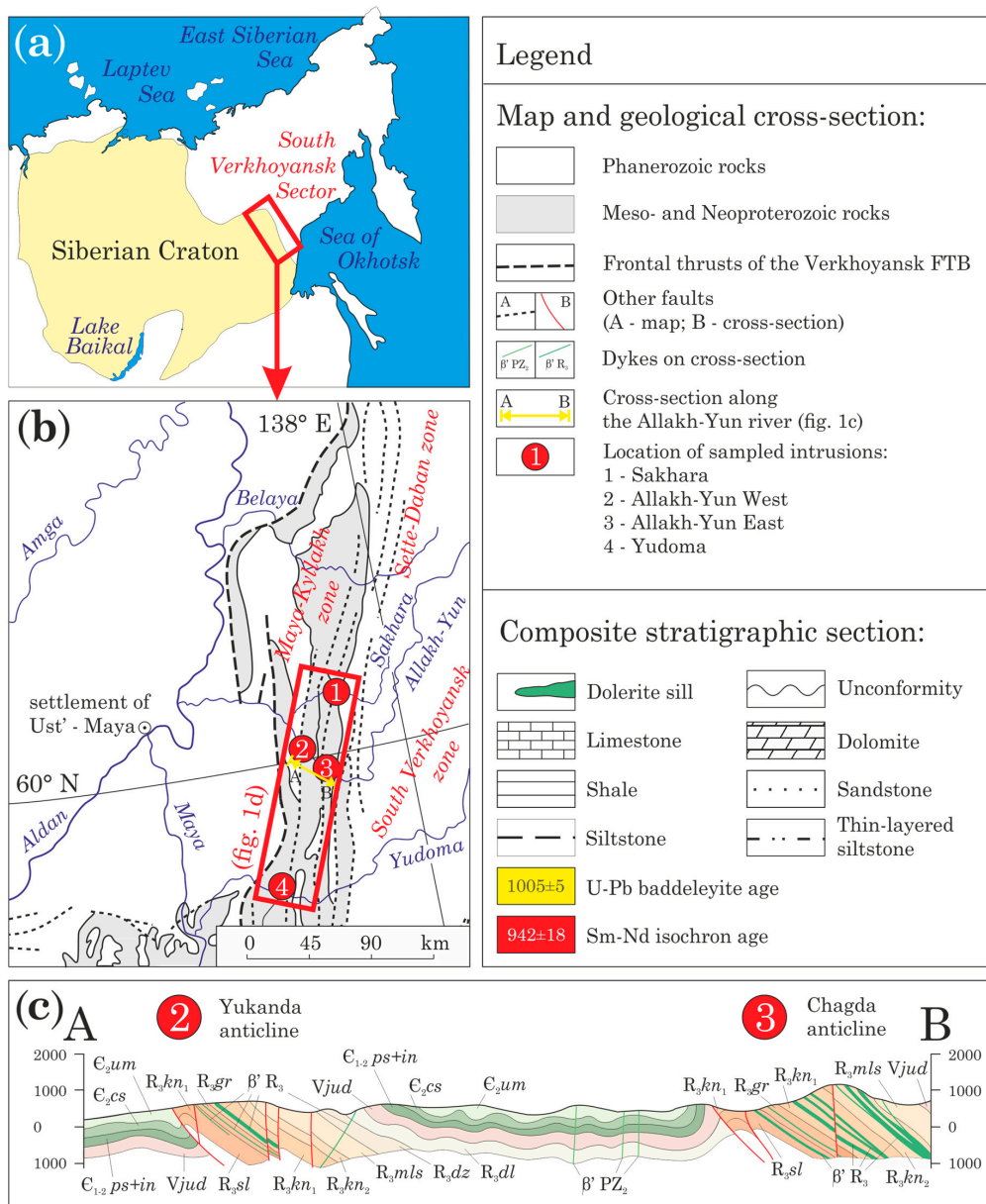


Figure 1. Cont.

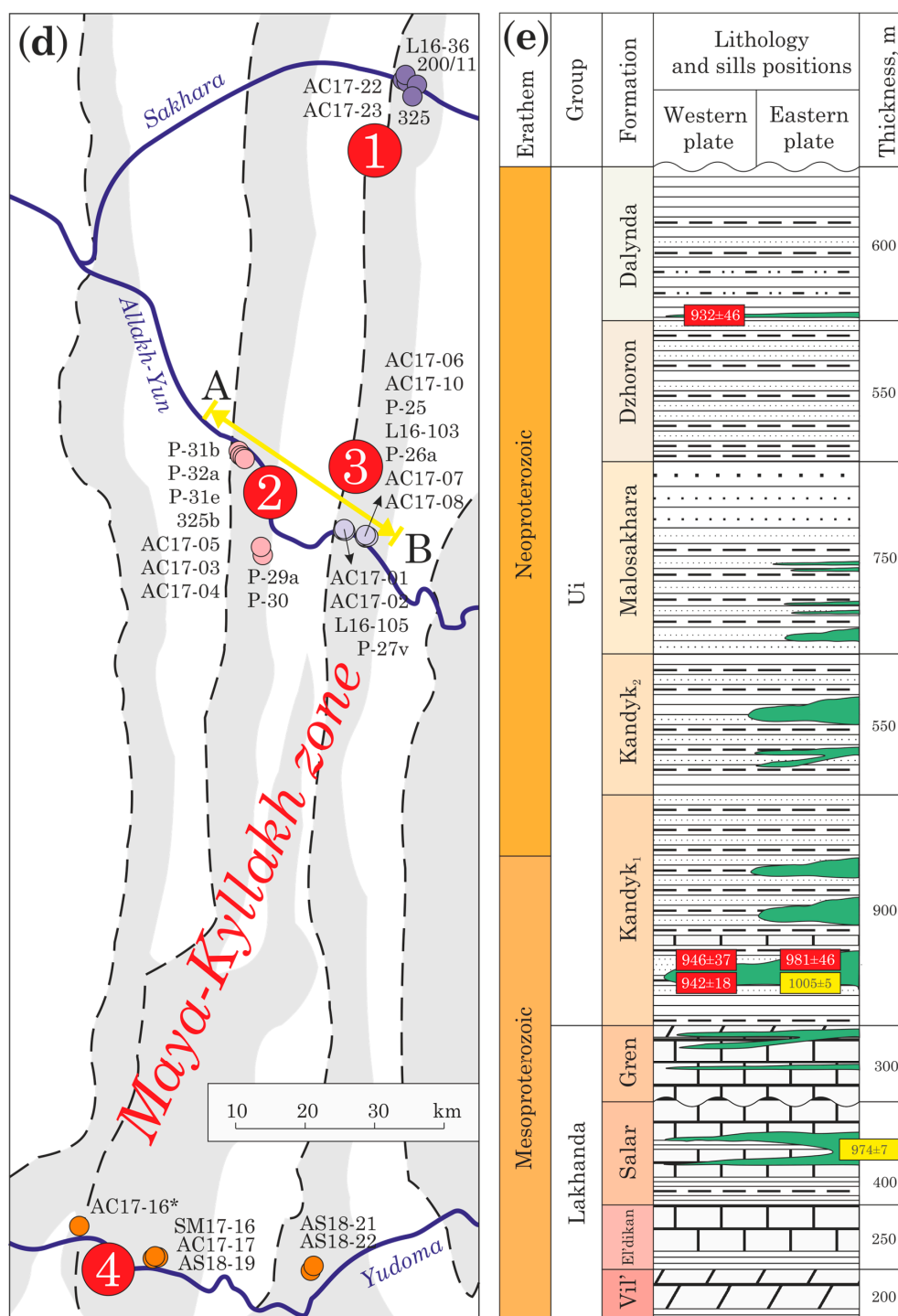


Figure 1. (a,b,d) Location maps, (c) cross-section (after [12], modified), and (e) composite stratigraphic section (after [12–14] and observations by authors) of the Meso- and Neoproterozoic succession in the Maya-Kyllakh zone. Sample locations, numbers, and specific colors used in the following diagrams are shown in Figure 1d. U-Pb baddeleyite and Sm-Nd isochron ages in Figure 1e are from [7,10,11].

2. Geological Setting and Petrography

The Verkhoyansk fold-and-thrust belt (Verkhoyansk FTB) is located along the eastern margin of the Siberian Platform, extending for 2500 km from the coast of the Laptev Sea in the north to the Sea of Okhotsk in the south. The outer zone of the Verkhoyansk FTB is divided (from north to south) into the Olenek, West Verkhoyansk, and South Verkhoyansk sectors [2]. The South Verkhoyansk sector

consists of three zones that include (from west to east) the Maya-Kyllakh, Sette-Daban, and South Verkhoyansk zones (Figure 1), composed of rocks of different ages and characterized by different structural styles [2,15].

Meso- and Neoproterozoic rocks intruded by mafic intrusions of the Sette-Daban event are only found in the Maya-Kyllakh zone. The geological structure of the Maya-Kyllakh zone is dominated by imbricate thrust sheets, with Meso- and Neoproterozoic rocks exposed in the hangingwalls of major thrusts (Figure 1c). The Meso- and Neoproterozoic succession contains several kilometer-scale distinctive siliciclastic-carbonate cycles. Most of these cycles are separated from each other by unconformities or erosional surfaces and have been mapped as groups. A detailed description of the sedimentary succession of the Sette-Daban region has been presented in several papers (e.g., [3,13,16]).

Our study is focused on the western and central parts of the Maya-Kyllakh zone, where only the Lakhanda, Uy, and Yudoma groups are exposed (Figure 1c). The Lakhanda Group consists of thick carbonate and shale units. U-Pb isochron dating of the carbonates yielded an age of 1020 ± 40 Ma, suggesting a latest Mesoproterozoic age for sedimentary rocks of the Lakhanda Group [17]. The Uy Group consists of fining-upward clastic rocks. Its lower part (Kandyk Formation) contains poorly-discordant detrital zircons as young as ca. 1050–1060 Ma, and was intruded by mafic sills with a U-Pb baddeleyite age of 1005 ± 4 Ma (Figure 1) [10,18]. The overlying Yudoma Group contains Ediacaran fossils (e.g., [13,16]).

Mafic sills of the Sette-Daban event are most widespread in the upper part of the Lakhanda Group and lower part of the Uy Group (Figure 1). Two intrusions were dated by the U-Pb baddeleyite method, yielding ages of 1005 ± 4 Ma (Sakhara river) and 974 ± 7 Ma (eastern part of the Allakh-Yun river, outside of the research area) [10]. Since the error margins associated with these ages do not overlap, it is possible that the Sette-Daban event was characterized by two episodes of magmatic activity, separated by a period of quiescence lasting at least 20 Myr. Sills from the west of the Allakh-Yun and Yudoma rivers yielded Sm-Nd ages of around 950 Ma (946 ± 37 , 932 ± 46 , and 942 ± 18 Ma [6,11]), which overlap within error with the 974 ± 7 Ma U-Pb baddeleyite age, and were likely intruded during the same phase of the Sette-Daban event. However, Sm-Nd isochron dating of a sill from the eastern part of the Allakh-Yun river was associated with a large error and dated as 981 ± 69 Ma [6], overlapping with both U-Pb baddeleyite ages.

The ages of sills exposed in thrust sheets in the Chagda anticline (eastern part of the Allakh-Yun river) and the Yukanda anticline (western part of the Allakh-Yun river) correlate with the ages of sills exposed along the Sakhara and Yudoma rivers, respectively. Therefore, we identify an older group of intrusions across the north-eastern part of the study area, which includes sills from the thrust sheets of the Sakhara river and eastern Allakh-Yun river (Chagda anticline), and a younger group of intrusions across the south-west of the study area, which includes sills from the thrust sheets of the western Allakh-Yun river (Yukanda anticline) and Yudoma river.

Intrusions of the Sette-Daban event are represented by dolerite sills and minor dikes. Lengths of the sills range from hundreds of meters to tens of kilometers, with thicknesses ranging from 2–3 m to 120–170 m (Figure 2).

The sills were intruded parallel to the bedding planes of host rocks and are characterized by chilled margins ranging in thickness from a few millimeters to 10 centimeters. The width of the baked margin zone is dependent on the thickness of the sill and typically ranges up to a few meters, but can also reach 15–20 m where dolerite sills are located in close proximity to each other. In the largest sills, the grain size increases from fine-grained to coarse-grained towards the upper contact of the intrusion [14].



Figure 2. Dolerite sill near the Sakhara river (sample AC17-22).

All of the studied intrusions comprise fine- to medium-grained dolerites and quartz dolerites, with grains ranging from 0.2 to 5 mm in diameter. The rock-forming minerals of the dolerites are dominated by plagioclase (An 50–70) and clinopyroxene (augite), comprising up to 90% of the thin section. The sampled dolerites are typically composed of plagioclase (27–45%) and augite (28–42%), with lesser amounts of hypersthene (3–8%), granophyric intergrowths of quartz and alkali feldspar (3–16%), biotite (1–7%), hornblende (2–5%), quartz (up to 4%), and olivine (up to 2%). The dolerites also contain accessory apatite (single grains) and ore minerals (5–14%), represented by magnetite, ilmenite, and titanomagnetite, the latter typically showing exsolved ilmenite.

A variety of textures are recognized in thin section (Figure 3), depending on intrusion size and position within the intrusion, including intergranular, poikilophitic, ophitic, doleritic, microdoleritic, and micrographic textures.

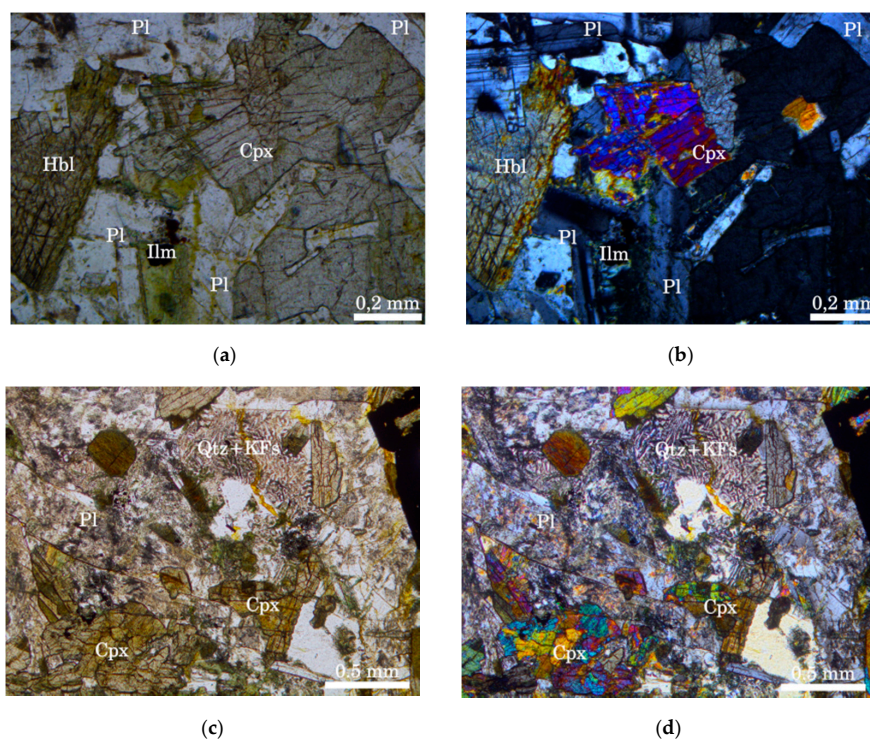


Figure 3. Photographs of thin sections in transmitted light (left column without analyzer, right column with analyzer), (a) and (b) sample AC17-07 (magnification $\times 10$) with gabbroophitic texture, (c) and (d) sample AC17-23 (magnification $\times 5$) with micrographic texture. Pl—plagioclase, Cpx—clinopyroxene, Hbl—hornblende, Ilm—ilmenite, Qtz—quartz, KFs—potassium feldspar.

Hydrothermal alteration can be recognized in most samples but the degree of alteration is variable. In approximately half of the samples, the alteration processes are not widely distributed and less than 10% of the rock-forming minerals are altered to secondary minerals. Plagioclase is locally replaced by sericite, albite, and epidote, whereas clinopyroxene is replaced by chlorite and amphibole (uralite). Plagioclase is typically more altered than clinopyroxene.

3. Analytical Methods

3.1. Whole-Rock Major and Trace Element Measurements

Whole-rock geochemical analyses were undertaken at the All Russian Geological Research Institute (VSEGEI) in St. Petersburg, Russia. Major element concentrations were determined by XRF using an ARL 9800 spectrometer, with trace and rare earth element (REE) compositions determined by inductively coupled plasma–mass spectrometry (ICP-MS) using an ELAN 6100 DRC ICP-MS. Measured concentrations were significantly above detection limits, with analytical uncertainties of <3% for major elements and 4–10% for trace elements and REE, except for Ni which had an uncertainty of about 15%. The international standards OU-6 and SBC-1 were used in this study. Concentrations of the major elements, trace elements, and REE, with detection limits for the studied samples, are given in Appendix A.

3.2. Whole-Rock Sm–Nd Isotope Measurements

The $^{147}\text{Sm}/^{144}\text{Nd}$ ratios and Nd isotope compositions were analyzed on a ThermoFisher Triton multi-collector TIMS at the Institute of Precambrian Geology and Geochronology (St. Petersburg), using the method described in [19]. The measured $^{143}\text{Nd}/^{144}\text{Nd}$ ratios were normalized to $^{146}\text{Nd}/^{144}\text{Nd} = 0.7219$ and adjusted to the La Jolla Nd standard ($^{143}\text{Nd}/^{144}\text{Nd} = 0.511860$). Total blank measurements during the analyses were 0.03–0.2 ng for Sm and 0.1–0.5 ng for Nd. Analytical error (2σ) was $\pm 0.5\%$ for the Sm and Nd concentrations, $\pm 0.5\%$ for the $^{147}\text{Sm}/^{144}\text{Nd}$ ratios, and $\pm 0.005\%$ for the $^{143}\text{Nd}/^{144}\text{Nd}$ ratios. $\epsilon_{\text{Nd}}(t)$ was calculated using the present-day ratios $^{143}\text{Nd}/^{144}\text{Nd} = 0.512638$ and $^{147}\text{Sm}/^{144}\text{Nd} = 0.1967$ in the chondritic uniform reservoir (CHUR) [20].

Sm–Nd isotope analyses for samples AS18-21 and AS18-22 were performed on a Finnigan MAT 262 mass spectrometer at the Geological Institute of the Kola Science Center RAS (Apatity), using the method described in [21]. The measured $^{143}\text{Nd}/^{144}\text{Nd}$ ratios were normalized to $^{146}\text{Nd}/^{144}\text{Nd} = 0.7219$ and adjusted to the La Jolla Nd standard ($^{143}\text{Nd}/^{144}\text{Nd} = 0.511860$). Total blank measurements during the analyses were 0.06 ng for Sm and 0.3 ng for Nd. Analytical error (2σ) was $\pm 0.5\%$ for the Sm and Nd concentrations, $\pm 0.5\%$ for the $^{147}\text{Sm}/^{144}\text{Nd}$ ratios, and $\pm 0.005\%$ for the $^{143}\text{Nd}/^{144}\text{Nd}$ ratios. $\epsilon_{\text{Nd}}(t)$ was calculated using the present-day ratios $^{143}\text{Nd}/^{144}\text{Nd} = 0.512638$ and $^{147}\text{Sm}/^{144}\text{Nd} = 0.1967$ in the CHUR [20]. The Sm–Nd isotope results are shown in Table 1.

Table 1. Whole-rock Sm–Nd isotope results. This study: IPGG (Institute of Precambrian Geology and Geochronology) and KSC (Kola Science Center RAS); Khudoley et al. [6]. See coordinates of samples in Appendix A.

Sample	Location	Lab	Age	Sm (ppm)	Nd (ppm)	$^{147}\text{Sm}/^{144}\text{Nd}$	$^{143}\text{Nd}/^{144}\text{Nd}$	$\epsilon(0)$	$\epsilon(t)$	Tdm	Tdm-2
AS18-21	Yudoma	KSC	950 (?)	3.115	9.705	0.19401	0.512806	3.3	3.7	2669	1351
AC17-10	AE	IPGG	981	7.11	25.29	0.1700	0.512688	1	4.4	1615	1287
AC17-4	AW	IPGG	946	2.307	6.677	0.2089	0.512958	6.3	4.8	6153	1263
P-25	AE	[6]	981	4.717	16.55	0.1723	0.512728	1.8	4.8	1558	1236
AS18-19	Yudoma	IPGG	942	3.178	9.362	0.2053	0.513014	7.4	6.3	2503	1081
AC17-17	Yudoma	IPGG	942	3.75	11.3	0.2007	0.513003	7.2	6.7	1744	1103
P-29a	AW	[6]	932	2.768	8.153	0.2052	0.513037	7.8	6.8	2061	1034
AC17-22	Sakhara	IPGG	1005	9.055	37.05	0.1478	0.512664	0.5	6.8	1128	1091
AS18-22	Yudoma	KSC	950 (?)	3.398	10.158	0.202165	0.513035	7.8	7.1	1543	1066
AC17-3	AW	IPGG	946	2.644	7.753	0.2062	0.513066	8.4	7.3	1746	1059
P-31e	AW	[6]	946	2.545	7.818	0.1967	0.513030	7.6	7.7	1091	972

4. Results

4.1. Major Elements

The intrusive igneous rocks associated with the Sette-Daban magmatic event display small variations in SiO_2 (46.76–51.99 wt%) and $\text{K}_2\text{O} + \text{Na}_2\text{O}$ (2.1–4.8 wt%), but larger variations in MgO (1.85–9.16 wt%), plotting in the moderately alkaline basalt field on the total alkali-silica (TAS) diagram (Figure 4a). All dolerites plot in the tholeiitic basalt field on the alkali- FeO_{tot} - MgO diagram (Figure 4b), lining up along the FeO - MgO axis. The Sakhara dolerites are characterized by the strongest Fe tholeiite signature, while the Yudoma dolerites are more calc-alkaline. The Mg\# increases from the Sakhara (0.13–0.38) to the Yudoma (0.41–0.51) samples, indicating the latter to be closer to the composition of primitive mantle melts. Dolerites from both the western and eastern Allakh-Yun river do not plot as two distinct groups, with their compositions overlapping those of the Sakhara and Yudoma samples.

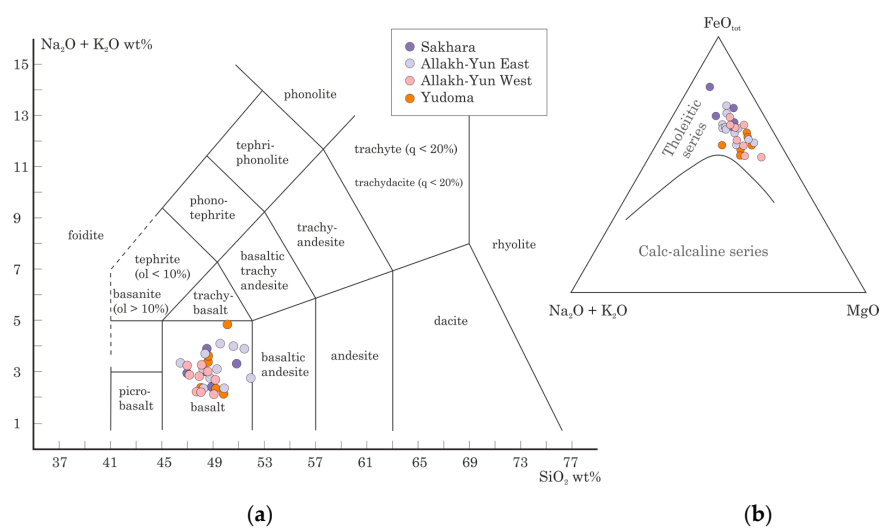


Figure 4. (a) Sette-Daban complex samples plotted on a total alkali-silica (TAS) diagram (after [22]). (b) Sette-Daban complex samples plotted on a $\text{Na}_2\text{O} + \text{K}_2\text{O}$ - FeO_{tot} - MgO discrimination diagram [23].

The Sette-Daban dolerites are characterized by low TiO_2 contents (1.17–2.86%) (Figure 5), corresponding to low titanium basalts. Due to their low MgO content of <8% and low Ni content, the observed variation in major element and Ni contents versus MgO content (Figure 5) can be considered as an effect of fractional crystallization.

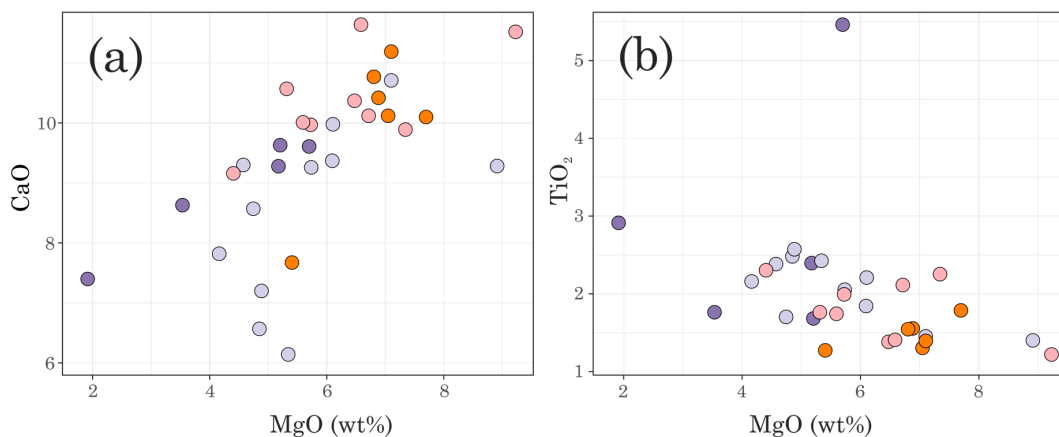


Figure 5. Cont.

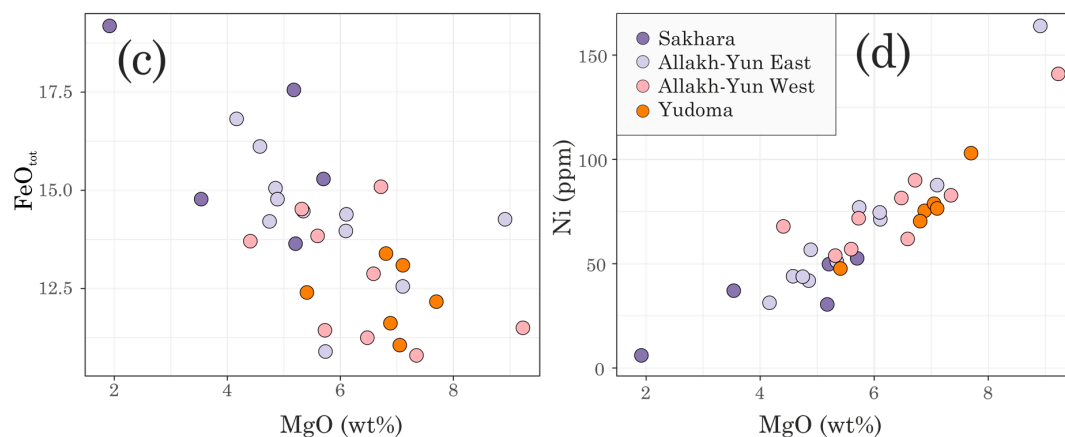


Figure 5. Plots of (a) CaO (wt%), (b) TiO₂ (wt%), (c) FeO_{tot} (wt%), and (d) Ni (ppm) vs. MgO (wt%) for the Sette-Daban event dolerites.

4.2. REE and Other Incompatible Elements

Major element compositions in a residual melt evolve as the crystallization of minerals such as plagioclase, olivine, or pyroxene takes place, hampering an interpretation of the original source of the melt based on major element compositions alone. However, the concentrations of highly incompatible large ion lithophile elements (LILE) and high field strength elements (HFSE), including rare earth elements (REE), are much less affected by fractional crystallization. Moreover, ratios of highly incompatible LILE are unaffected by fractional crystallization, with ratios primarily controlled by the degree of partial melting [24]. Therefore, in order to constrain the partial melting process of the mantle source, we focus on ratios of highly incompatible LILE in the discussion below.

Samples from the Sakhara and eastern Allakh-Yun rivers show an enrichment in light rare earth elements (LREE) over heavy rare earth elements (HREE) [(La/Yb)_N = 1.58–3.35] and weak Eu depletion (Figure 6a).

Primitive mantle- (PM-) normalized trace element patterns (Figure 6b) of the Sakhara and eastern Allakh-Yun dolerites exhibit some variations in LILE and a generally pronounced enrichment in LREE, a wide range in Th and U, weak negative Ta-Nb anomaly, negative Sr, and positive Pb anomaly. The PM-normalized trace element patterns for the Sakhara and eastern Allakh-Yun dolerites demonstrate a closer similarity to island arc basalts (IAB) [24] than to ocean island basalts (OIB) or mid-ocean ridge basalts (MORB). The negative Sr and weak negative Eu anomalies in those dolerites can be explained by the buffer effect of crystallizing plagioclase. The positive Pb anomaly is related to recycled sediment in the melting mantle source [25].

The Yudoma and western Allakh-Yun dolerites display flat REE patterns and lack a negative Eu anomaly, similar to the composition of normal mid-ocean ridge basalt (N-MORB) (Figure 6a). The lower (La/Yb)_N ratio (0.73–1.18) in the Yudoma and western Allakh-Yun dolerites, compared to the Sakhara and eastern Allakh-Yun dolerites, may be related to differences in the degree of partial melting of the mantle source.

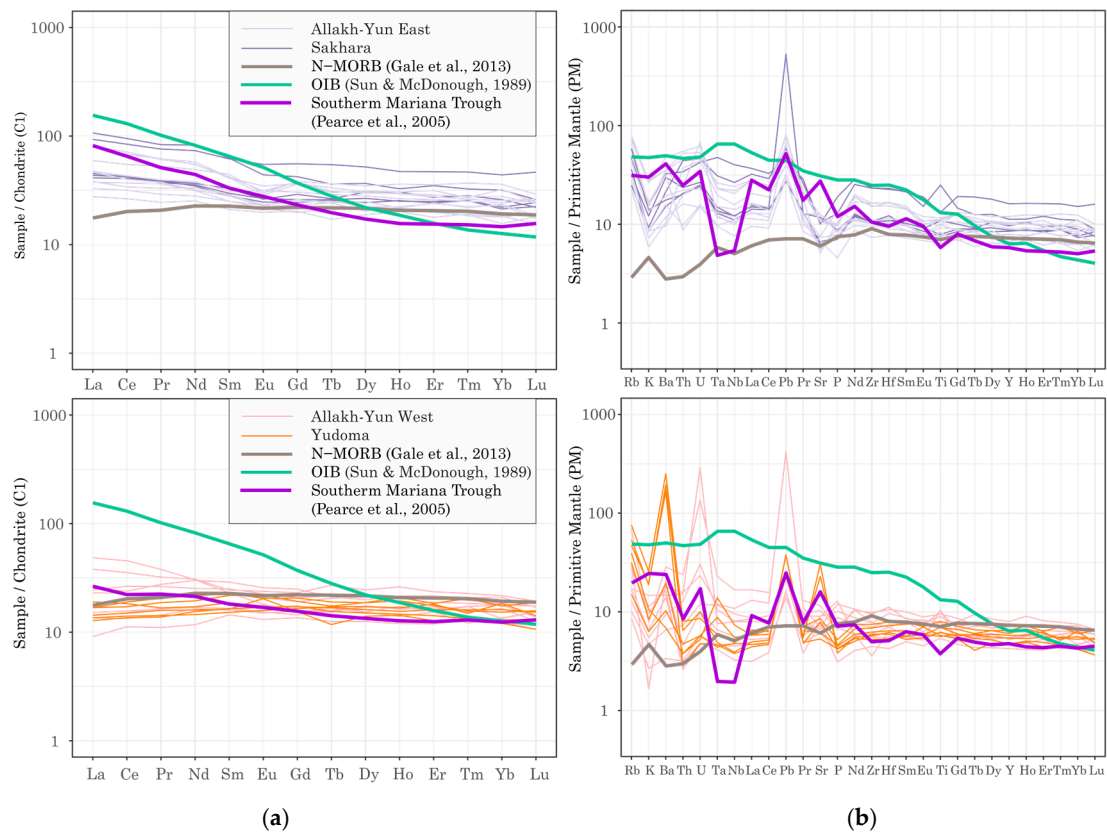


Figure 6. (a) Chondrite-normalized rare earth elements (REE) plot and (b) primitive mantle-normalized trace element diagram for the Sette-Daban magmatic event intrusions. The trace element compositions of ocean island basalts (OIB), along with chondrite and primitive mantle normalization values, are from [26]. The trace element compositions of normal mid-ocean ridge basalt (N-MORB) are from [27]. Trace element compositions of the southern Mariana Trough are from [24].

The dolerites from Yudoma and western Allakh-Yun are characterized by large ranges in concentrations of most incompatible elements. With the exception of two samples, all dolerites from these areas more closely resemble N-MORB in relation to immobile (IM) incompatible trace element concentrations (Th, Nb). However, at the same time, they are characterized by a very high enrichment in high-fluid-mobility (HFM) incompatible trace elements (Ba, U, Sr, Pb) [28,29], which could reflect a shallow subducted sediment component [24,28].

4.3. Nd Isotopes

All four dolerite groups do not show significant variations in Nd isotope compositions (Figure 7). $\epsilon_{\text{Nd}}(t)$ values range from 3.6 to 7.5, indicating a depleted MORB source with a minor contribution from an enriched source. The Nd isotope compositions of most samples do not exhibit a clear correlation with SiO_2 contents (Figure 7b), implying that direct crustal contamination, as suggested by the range of Nd isotope values, is very unlikely. However, samples from the Yudoma river group demonstrate a weak negative correlation between $\epsilon_{\text{Nd}}(t)$ and SiO_2 . Therefore, we cannot completely exclude the possibility of a minor amount of direct crustal contamination. Nevertheless, the small variation in $\epsilon_{\text{Nd}}(t)$, as well as in the chemical composition of the dolerites, allow us to suggest that the effect of possible crustal contamination on the primitive geochemical pattern of the dolerites is likely to be insignificant.

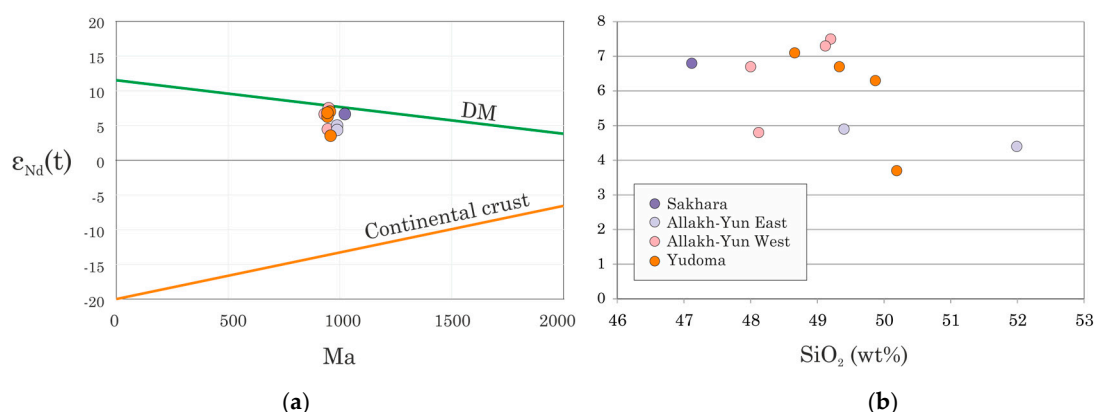


Figure 7. (a) $\epsilon_{Nd}(t)$ —age (Ma) plot. (b) $\epsilon_{Nd}(t)$ — SiO_2 (wt%) plot.

5. Discussion

5.1. LILE Variations in Contributions from Aqueous Fluids

Alteration of the mafic rocks is minor, and when optically discernible, appears to mostly affect plagioclase, forming sericite, albite, and epidote. Such alteration is too small to affect the chemical composition of the rocks. Nevertheless, it could affect the primordial trace element abundance in the studied dolerites, especially fluid mobile trace elements such as Rb, Sr, Ba, and U. We used the loss on ignition (LOI) value to test the effect of post-crystallization alteration and weathering on the primordial content of highly mobile elements in the dolerites (Figure 8). The absence of a correlation between mobile elements and LOI indicates that no alteration occurred after crystallization, therefore the variation in Ba-Sr-U could be related to metasomatic alteration of the melting source. At the same time, several samples (e.g., ##AS18-21, AS18-22, AC17-16*) contain anomalously high concentrations of Sr and Ba, along with high LOI values. In addition, significant enrichments in Ba, Sr and U in those samples are not accompanied by enrichments in other highly incompatible elements (such as Rb, K, Th, U, La, Ce). Consequently, the geochemical peculiarities of these samples could have been generated by secondary alteration processes. Therefore, samples with an anomalously high enrichment in Ba, Sr, and U should be excluded from the discussion concerning HFM incompatible trace elements. The other samples demonstrate no obvious correlation of LILE concentration with LOI value and can be assumed to have undergone no post-crystallization alteration.

The enrichment in, and wide variation of, HFM elements in the observed dolerites could be explained as a result of the fertilization of lithospheric mantle by aqueous fluids at shallow depths prior to melting [24,30]. The ratios of mobile-to-immobile incompatible trace elements which have similar bulk partitioning coefficients (e.g., Ba/Th, Sr/Th) do not considerably fractionate during mantle melting and following fractional crystallization [31]. Therefore, any variation in their ratios can be interpreted to reflect geochemical heterogeneity of the mantle. On the other hand, LILE are soluble in aqueous fluids and any variations in Ba/Th and Sr/Th ratios are likely to reflect the secondary impact of aqueous fluids (metasomatism) on the composition of the mantle source [32,33]. On the plots of Ba/Th and Sr/Th versus Th/Nd (Figure 9), the analyzed dolerites form similar negatively correlated trends, indicating the importance of aqueous fluids for the generation of basaltic magma. The Yudoma and some of the western Allakh-Yun dolerites are characterized by higher Ba/Th and Sr/Th compared to those from the Sakhara and eastern Allakh-Yun, suggesting that they may be associated with larger contributions from aqueous fluids in the melting source. We suggest that the variations in contributions from aqueous fluids are associated with different depth levels of subduction-related alteration of the lithospheric mantle, including shallow depths for the source of the Yudoma dolerites, and deeper levels for the source of the Allakh-Yun and Sakhara dolerites [24].

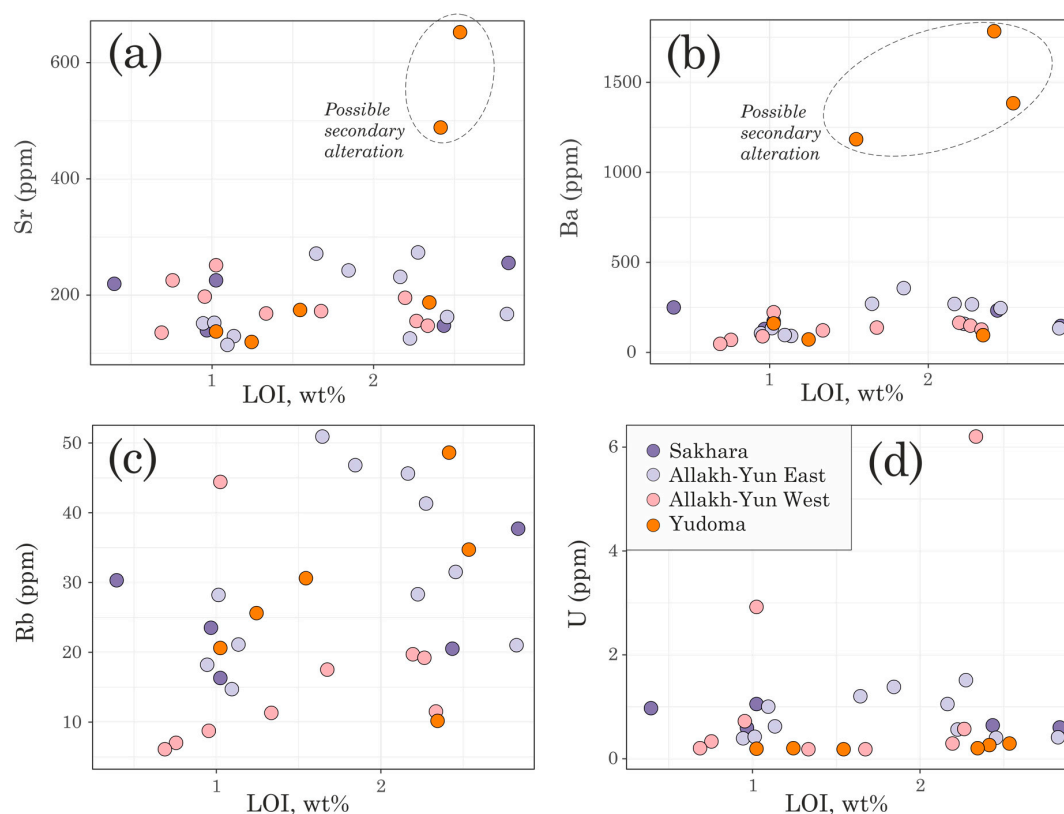


Figure 8. Plots of (a) Sr (ppm), (b) Ba (ppm), (c) Rb (ppm), and (d) U (ppm) vs. loss on ignition (LOI) (wt%) for the Sette-Daban event dolerites.

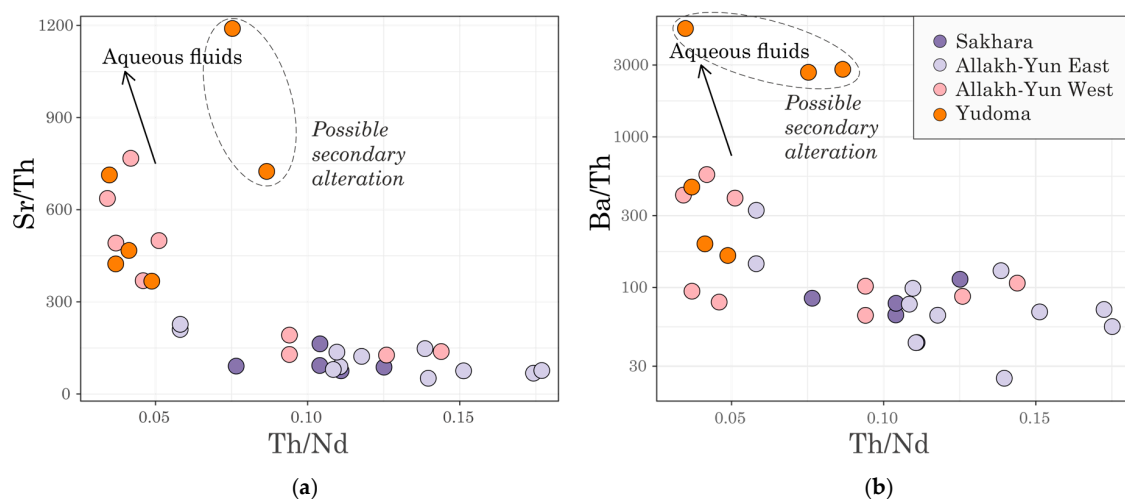


Figure 9. Plots of (a) Sr/Th vs. Th/Nd and (b) Ba/Th vs. Th/Nd for the Sette-Daban event dolerites.

5.2. Immobile Incompatible Trace Element Variations and the Mantle Source

On the Th/Yb–Nb/Yb plot, the Sette-Daban sills can be subdivided into two groups based on distinct geochemical compositions (Figure 10a). The first group plots within the mantle MORB–OIB array, mostly comprising dolerites from the Yudoma and western Allakh-Yun rivers, but also a few samples from Sakhara and eastern Allakh-Yun. Variations within the mantle array on the Th/Yb–Nb/Yb plot reflect differences in the degree and depth of melting, whereby the Sakhara sample is the most differentiated and the Yudoma samples are the most primitive. The second group of samples mostly

comprises dolerites from the Sakhara and eastern Allakh-Yun rivers, along with a few samples from Yudoma and western Allakh-Yun, and are shifted out of the mantle array towards the volcanic arc array. This contrasting geochemical composition suggests that the mantle source of the second dolerite group experienced crustal contamination or subduction-related modification [25]. The second group also plots within the volcanic arc field on the Nb/Th–Zr/Nb plot (Figure 10b). The western and eastern Allakh-Yun dolerites appear to encompass the range of compositions defined by the Sakhara and Yudoma sills, but the eastern sills more closely resemble Sakhara signatures, whereas the western sills more closely resemble Yudoma signatures. It is difficult to explain the observed variations in ratios of immobile incompatible trace elements (especially Nb/Th) by partial melting, but these variations could be explained by the addition of incompatible trace elements to the lithospheric mantle at deep depths during subduction, analogous to the modern Mariana Trough [24].

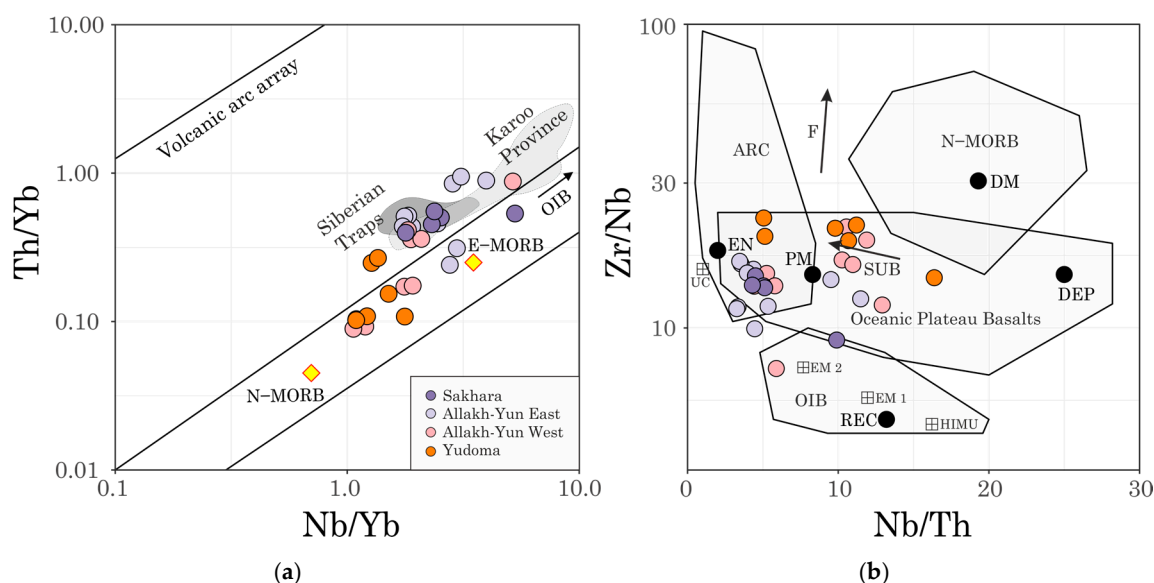


Figure 10. (a) Th/Yb–Nb/Yb plot [34,35]. The composition of the Siberian Traps (dark gray field) is taken from [36], while the composition of the Karoo Province is taken from [37]. (b) Zr/Nb–Nb/Th plot [38]. Abbreviations: UC—upper continental crust; PM—primitive mantle; DM—shallow depleted mantle; HIMU—high mu (U/Pb) source; EM 1 and EM 2—enriched mantle sources; ARC—arc-related basalts; N-MORB—normal mid ocean ridge basalt; OIB—oceanic island basalt; DEP—deep depleted mantle; EN—enriched component; REC—recycled component. Arrows indicate effects of batch melting (F) and subduction (SUB). References: [39,40].

Another key difference between the two groups of dolerites is their contrasting REE patterns (Figure 6), best illustrated by their LREE/MREE (middle REE) fractionation systematics. Fractionation of LREE/MREE and MREE/HREE allows us to understand the melting regime in the mantle [37]. All of the dolerite samples demonstrate obvious fractionation between the LREE/MREE ratios, while fractionation between the MREE/HREE ratios is not observed (Figure 6a). The La/Sm and Sm/Yb ratios do not correlate with Mg-number and their variations cannot be explained by fractional crystallization or crustal contamination processes [37].

The diagram in Figure 11 displays model trends of peridotite melting corresponding to different physical parameters and representing compositions of aggregated melts. OIB compositions form at high pressures and high potential temperatures, characteristic of a mantle plume, while MORB compositions reflect melting of the mantle at relatively shallow depths and lower temperatures. The Sette-Daban dolerites are characterized by an almost flat Sm/Yb trend, corresponding to melting at relatively low pressures, with increasing temperatures from the eastern Allakh-Yun and Sakhara dolerites to the Yudoma and western Allakh-Yun dolerites. All samples plot well within the MORB

field, which is consistent with their low alkali and low Ti compositions, which are noticeably distinct from OIB compositions on the Th/Yb–Nb/Yb plot (Figure 10a). The Sm/Yb and La/Sm ratios also exclude the presence of garnet in their melt source, suggesting melting of a shallower spinel-bearing source [37] with different degrees of melting or subduction-related modification, as inferred from the Th/Yb–Nb/Yb diagram (Figure 10a).

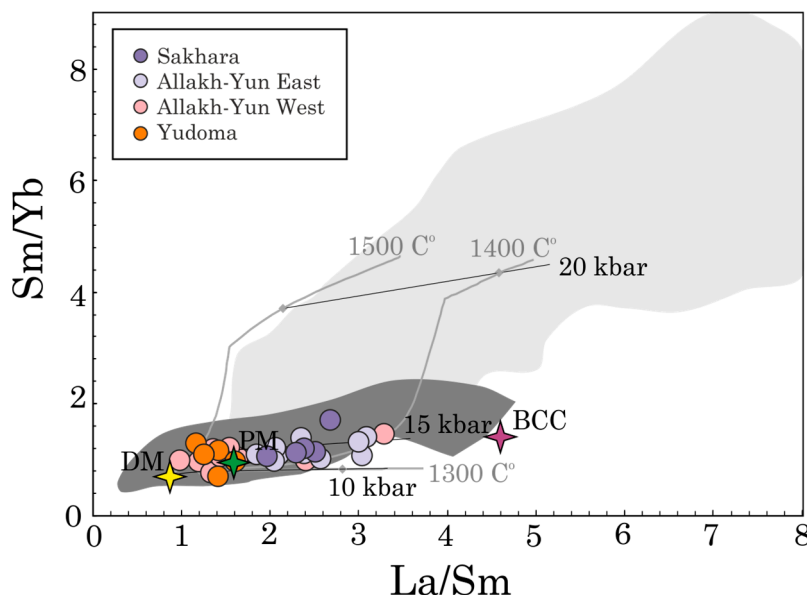


Figure 11. La/Sm–Sm/Yb plot with P – T conditions of melting. Solid grey lines represent segregated melt compositions formed during the melting of mantle peridotite at various pressures (gray rhombs connected by black lines), and correspond to different potential temperatures. The model composition of segregated peridotite melts was calculated in the AlfaMelts program code [41], using mineral–melt distribution coefficients for rare elements from [42]. The evolutionary trends calculated for the melting of peridotite correspond to DM composition. The composition of depleted mantle (yellow star) is taken from [43]. The composition of primitive mantle (green star) is taken from [44]. BCC (violet star) represents the composition of bulk continental crust [45]. The dark gray field represents the compositional range of MORB basalts, while the pale grey field represents the compositional range of OIB basalts [46].

The studied samples can be geographically separated into the “northern” (Sakhara) and “southern” (Yudoma) groups based on their incompatible trace element ratios (Th/Yb, Nb/Yb, Nb/Th, La/Sm; Figures 10 and 11). A transitional zone between the two groups includes the sub-latitudinal profile of the Allakh-Yun river, encompassing geochemical features of both the Sakhara and Yudoma areas. The geochemical differences between the “southern” and “northern” dolerite patterns are also apparent in the mobile LILE concentrations (Ba, Sr, U, Pb) (Figure 9), suggesting lateral heterogeneity of the lithospheric mantle/melting source. By integrating all of the geochemical characteristics, we suggest that the Yudoma (southern) mantle source composition was modified by metasomatic enrichment induced by hydrous fluid alteration and expressed in fluid mobile LILE, possibly reflecting ancient subduction at shallow depths [24]. On the other hand, the Sakhara (northern) mantle source is enriched in immobile incompatible elements (Th, Nb and LREE) induced by the melting of recycled sediments, possibly reflecting alteration by ancient subduction at deeper levels [24]. The variation in initial Nd isotope signatures of the studied dolerites can be explained by subduction-related alteration of their mantle source.

5.3. Tectonic Settings of Sette-Daban Magmatism

The dolerite sills of the Sette-Daban magmatic event are distributed along the south-eastern margin of the Siberian Craton and were intruded into Meso-Neoproterozoic sedimentary cover of the Siberian passive margin, based on ages of around 975–1000 Ma determined from U-Pb dating of baddeleyite [1–4,6,10]. During this time, Siberia formed part of a supercontinent, along with Laurentia and Baltica [47–49]. The Sette-Daban region was located far from any lithospheric plate boundaries [3], and its magmatic activity can be considered as intraplate volcanism induced by continental rifting. Despite the paleo-tectonic position of the studied intrusions, trace element patterns of the dolerites have common features to those characteristic of island arc settings (IAB). IAB-like geochemical features could be generated by a post-orogenic mafic magmatic event or intraplate LIP. Post-orogenic rifting and delamination is often followed by the development of mafic magmatism bearing IAB-like geochemical features [50]. Based on numerous paleogeographic reconstructions, Siberia was connected to Laurentia at 1000 Ma when the large Grenvillian orogenic event occurred [10,11,47,49]. Nonetheless, post-orogenic mafic magmatic rocks are typically characterized by high alkalinity (presumably potassic), along with high Ti and LILE concentrations (e.g., [51]), far exceeding those of the Sette-Daban dolerites.

On the other hand, trace element patterns of the Sette-Daban dolerites resemble those of low-Ti basic lavas and dikes of intraplate large igneous provinces (LIP), such as the Early Jurassic Karoo Province and Permian–Triassic Siberian Traps flood basalts [36,37] (Figure 10a). A number of models have been proposed for the origins of LIP ([52] and references therein), with at least two models proposed for the origins of the Karoo and Siberian provinces. The low-Ti basalts of the Karoo province are considered to have formed as a result of plume-lithosphere interaction. The low Ti content and IAB-like trace element pattern could be explained by the geochemical peculiarity of the sub-continental lithospheric mantle, acquired prior to the development of an intracontinental tectonic setting [37]. Thus, the metasomatic enrichment of sub-continental lithospheric mantle could be associated with ancient subduction. This enriched mantle was apparently preserved beneath the craton until continental rifting initiated melting during the Sette-Daban event.

A more recent model for the Siberian Traps flood basalt magmatism assumes long-term subduction beneath the lithospheric plate on which the intraplate magmatic event occurred. This model invokes mantle melting and subsequent intraplate magmatism, as a result of deep water and fluid recycling due to ongoing crustal subduction [36,52]. Geochemical features, such as negative Ta-Nb anomalies and contamination by incompatible elements (Th, Pb), could be explained by the recycling of terrigenous sediments aboard the subducting slab. Support for the involvement of a previous subduction event in the mantle source of the Sette-Daban magmatism can be acquired from the preceding Grenville active margin, with subsequent continental collision along convergent plate boundaries located across Laurentia, Baltica and Siberia from 1.4 to 1.0 Ga [10,47,53]. On the contrary, the geodynamic context for intraplate mafic magmatism can explain the shallow depth of melting revealed by the La/Sm and Sm/Yb ratios, as well as the flat REE patterns of the studied dolerites. In light of our new data, we suggest that the Sette-Daban intrusions were formed by melting of depleted MORB mantle (DMM), enriched by subduction-related components. To test the various hypotheses proposed above, further geochemical, Sr-Nd-Pb isotope, and geochronological data are urgently required.

6. Conclusions

Our new geochemical and Nd isotope data for dolerite sills from Sette-Daban (South Verkhoyansk region, eastern Siberia), provide new constraints on the mantle source which formed the latest Mesoproterozoic to early Neoproterozoic mafic intrusions of the Sette-Daban province.

The major and trace element data, along with initial Nd isotope compositions, obtained for the Sette-Daban dolerites allow us to propose the following conclusions:

- The Sette-Daban dolerite sills resemble low-Ti lavas of intraplate flood basalt provinces (e.g., Karoo, Siberian Traps) and possess IAB-like trace element patterns.

- The studied dolerites are the magmatic products of shallow-depth melting of depleted sub-continental lithospheric mantle, due to continental rifting.
- The trace element compositions of intrusions across the study area reveal striking geochemical differences between northern and southern sills, reflecting lateral heterogeneity in the composition of their mantle source.
- The source for both northern and southern sills was depleted lithospheric mantle, metasomatically enriched at different depths by ancient subduction.

Author Contributions: Conceptualization, A.D.S. and S.V.M.; formal analysis, V.M.S.; investigation, A.D.S., S.V.M., V.M.S. and D.D.I.; writing—original draft preparation, A.D.S.; writing—review and editing, S.V.M. and A.D.K.; visualization, A.D.S. and A.D.K.; funding acquisition, A.D.S. and S.V.M. All authors have read and agreed to the published version of the manuscript.

Funding: Nd isotopes analysis of samples AS18-21 and AS18-22 has been carried out within the mega-grant in accordance with Resolution of the RF Government (Agreement No. 14.Y26.31.0012). Other studies were funded by the Russian Science Foundation, grant number 19-77-10048.

Acknowledgments: This manuscript was improved after insightful reviews by an anonymous referee. We are grateful to Galina Kazakova and Olga Lebedeva from A.P. Karpinsky Russian Geological Research Institute for research materials support as well as Andrei Khudoley (St. Petersburg State University) for valuable discussion. Authors are grateful to James Barnett for useful comments on the first draft of the paper and correcting the English.

Conflicts of Interest: The authors declare no conflict of interest.

Appendix A

Table A1. The results of whole-Rock Major and Trace Element Measurements.

Sample	Location	Latitude	Longitude	SiO ₂ %	Al ₂ O ₃ %	TiO ₂ %	Fe ₂ O _{3tot} %
AC17-22	Sakhara	60°43′09.8″	136°59′19.8″	47.08	11.61	5.409	16.87
AC17-23	Sakhara	60°43′10.1″	136°59′19.9″	48.96	11.47	2.342	19.39
L16-36	Sakhara	60°43′21.9″	136°59′38.9″	50.9	10.8	2.86	21.2
200/11	Sakhara	60°43′01.4″	137°01′07.0″	48.6	13.9	1.71	16.3
325	Sakhara	60°41′39.8″	137°00′10.8″	48.6	14.03	1.63	15.04
AC17-01	Allakh-Yun east	60°12′58.4″	136°50′57.8″	51.51	12.99	2.372	15.96
AC17-02	Allakh-Yun east	60°12′57.7″	136°51′01.6″	50.63	13.05	2.429	16.61
AC17-06	Allakh-Yun east	60°12′30.8″	136°53′41.9″	48.85	12.96	2.156	15.87
AC17-10	Allakh-Yun east	60°12′33.0″	136°53′29.1″	51.99	11.29	2.106	18.57
P-25	Allakh-Yun east	60°12′40.0″	136°53′38.4″	49.4	15	2	11.99
L16-103	Allakh-Yun east	60°12′32.7″	136°53′31.4″	48.3	12.1	2.33	17.79
P-26a	Allakh-Yun east	60°12′23.4″	136°54′10.8″	48.5	13.3	1.65	15.67
L16-105	Allakh-Yun east	60°12′57.8″	136°51′00.1″	49.6	13	2.52	16.3
P-27v	Allakh-Yun east	60°13′14.2″	136°51′00.0″	46.51	15.07	1.79	15.4
AC17-07	Allakh-Yun east	60°12′42.5″	136°53′04.2″	49.9	13.81	1.4	13.83
AC17-08	Allakh-Yun east	60°12′37.0″	136°53′22.6″	48.31	13.1	1.348	15.73
P-31b	Allakh-Yun west	60°18′02.6″	136°38′34.0″	47.1	13.9	1.71	16.02
P-32a	Allakh-Yun west	60°18′12.6″	136°38′16.8″	48.6	15.6	1.94	12.59
P-31e	Allakh-Yun west	60°18′02.6″	136°38′34.0″	49.2	14	2.25	15.11
325b	Allakh-Yun west	60°18′12.6″	136°38′16.8″	47.29	14.58	1.69	15.26
AC17-05	Allakh-Yun west	60°18′30.7″	136°37′59.2″	47.76	13.74	2.06	16.65
P-29a	Allakh-Yun west	60°11′42.1″	136°39′31.0″	48	15.6	1.33	12.38
P-30	Allakh-Yun west	60°11′09.2″	136°40′19.9″	48.2	14	2.2	11.8837
AC17-03	Allakh-Yun west	60°18′01.5″	136°38′36.6″	49.12	14.34	1.355	14.19
AC17-04	Allakh-Yun west	60°18′24.8″	136°38′09.3″	48.12	13.46	1.167	12.66
AS18-21	Yudoma	59°23′40.7″	136°47′15.6″	50.19	14.35	1.22	13.66
AS18-22	Yudoma	59°23′51.3″	136°47′29.0″	48.66	14.72	1.502	12.79
AC17-16*	Yudoma	59°25′55.1″	136°16′30.1″	48.71	14.5	1.252	12.17
AC17-17	Yudoma	59°23′34.6″	136°25′40.7″	49.33	12.97	1.734	13.4
AS18-19	Yudoma	59°23′41.8″	136°25′55.7″	49.87	13.07	1.492	14.76
SM17-16	Yudoma	59°23′41.1″	136°25′55.9″	48.14	14.1	1.342	14.43
LOD *	-	-	-	0.02	0.05	0.01	0.01

LOD *—limit of detection. Major element concentrations were determined by XRF using an ARL 9800 spectrometer. Values are given in oxide weight percent.

Table A2. The results of whole-Rock Major and Trace Element Measurements (continuation).

Sample	MnO%	MgO%	CaO%	Na ₂ O%	K ₂ O%	P ₂ O ₅ %	LOI%	Σ%	* Mg#
AC17-22	0.2394	5.634	9.539	2.025	0.9295	0.4115	0.37	100	0.37
AC17-23	0.2888	5.11	9.209	1.908	0.5198	0.1536	0.943	100	0.32
L16-36	0.31	1.85	7.33	2.77	0.56	0.28	1.55	98.86	0.13
200/11	0.23	3.47	8.56	3.07	0.84	0.19	2.81	99.68	0.27
325	0.24	5.14	9.56	2.3	0.73	0.16	2.41	99.84	0.38
AC17-01	0.1936	5.277	6.071	2.35	1.575	0.2126	1.82	100	0.37
AC17-02	0.232	4.785	6.498	2.361	1.634	0.2139	1.62	100	0.34
AC17-06	0.2318	6.04	9.908	2.24	0.514	0.1957	1.11	100	0.40
AC17-10	0.233	4.097	7.75	2.408	0.3542	0.2285	1.07	100	0.28
P-25	0.21	5.67	9.19	2.61	0.52	0.3	2.8	99.69	0.46
L16-103	0.29	4.51	9.23	2.32	0.81	0.16	2.17	100.01	0.31
P-26a	0.25	4.68	8.5	2.79	0.92	0.18	2.25	98.69	0.35
L16-105	0.24	4.82	7.13	2.42	1.7	0.21	2.14	100.08	0.34
P-27v	0.26	6.03	9.3	2.35	1	0.17	2.43	100.31	0.41
AC17-07	0.215	7.037	10.64	1.921	0.4362	0.0989	0.92	100	0.48
AC17-08	0.24	8.847	9.212	1.722	0.6516	0.1008	0.989	100	0.50
P-31b	0.24	5.25	10.5	2.79	0.47	0.15	1	99.13	0.37
P-32a	0.22	5.66	9.9	2.67	0.33	0.22	0.93	98.66	0.44
P-31e	0.28	4.34	9.09	2.6	0.1	0.28	2.17	99.42	0.34
325b	0.21	5.53	9.94	2.33	0.57	0.26	2.24	99.9	0.39
AC17-05	0.2415	6.651	10.05	1.965	0.2827	0.1436	0.731	100	0.42
P-29a	0.21	6.41	10.3	2.45	0.39	0.15	1.31	99.7	0.48
P-30	0.16	7.28	9.82	2.41	0.88	0.19	2.311	100.1	0.52
AC17-03	0.2263	6.52	11.57	1.967	0.161	0.0904	0.663	100	0.45
AC17-04	0.1962	9.163	11.45	1.545	0.6801	0.0674	1.65	100	0.56
AS18-21	0.2254	5.341	7.603	3.308	1.541	0.0973	2.39	99.93	0.41
AS18-22	0.2133	6.819	10.35	2.223	1.155	0.0925	1.52	100	0.49
AC17-16*	0.1831	6.984	10.05	2.529	1.133	0.0829	2.51	100	0.51
AC17-17	0.1892	7.632	10.03	1.998	0.3794	0.1135	2.32	100	0.50
AS18-19	0.2503	6.74	10.7	1.677	0.5064	0.1	1	100	0.45
SM17-16	0.2285	7.038	11.12	1.778	0.6384	0.092	1.22	100	0.46
LOD	0.01	0.1	0.01	0.1	0.01	0.05	0.1	-	-

* Mg# = $\frac{\text{MgO}/40.32}{\text{MgO}/40.32 + \text{Fe}_2\text{O}_{3\text{tot}}/71.8}$ Major element concentrations were determined by XRF using an ARL 9800 spectrometer. Values are given in oxide weight percent.

Table A3. The results of whole-Rock Major and Trace Element Measurements (continuation).

Sample	Sc	V	Cr	Co	Ni	Rb	Sr	Y	Zr	Nb	Ba	La	Ce	Pr	Nd
AC17-22	49.7	628	61	43.9	50.6	29.7	212	51.1	261	28.6	226	25.3	58.1	7.91	38.6
AC17-23	52.7	563	4.56	55.8	28.5	22.9	132	43.8	117	7.88	106	9.76	24.9	3.67	17.1
L16-36	41.4	94.5	-	37.5	4.07	15.7	218	73.4	260	18.9	149	22.1	51.5	7.21	34.3
200/11	32.1	413	239	47.4	35.1	37.1	248	39.6	118	8.7	123	10.3	25.8	3.54	16.6
325	38.6	413	76.7	47.6	47.8	19.9	140	38.7	119	8.56	209	10.7	25.7	3.66	16.2
AC17-01	45.1	457	46.5	52.8	49.1	46.2	235	46.9	183	15.6	333	19.1	43.6	5.83	27
AC17-02	43.1	440	32.6	44.9	39.9	50.3	264	45	169	14.6	246	19.1	41.5	5.87	25.5
AC17-06	45	404	127	48.3	69.3	20.5	122	35.9	116	7.43	67.4	9.04	20.8	3.14	15.6
AC17-10	43.4	457	9.48	49.3	29.3	14.1	107	54.4	182	11.2	72.7	14.1	33.5	5.02	22.9
P-25	37	293	93	42.9	75	20.4	160	34	114	7.9	110	8.91	22.6	3.45	14.7
L16-103	50.3	560	-	55	42	27.7	118	41	119	10.1	135	11.2	26.3	3.74	17.7
P-26a	-	370	26.6	42.4	41.8	40.7	266	32.7	117	7.06	243	11	24.5	3.56	14.9
L16-105	45.4	487	-	46.7	54.7	45	224	45.4	171	17.2	245	19.3	43.4	5.78	25.8
P-27v	40.4	384	114	51.8	72.6	30.9	155	30.3	106	8.46	222	7.82	19.4	2.76	13.1
AC17-07	47.3	379	238	50.8	85.7	17.6	144	28.2	82.4	5.43	82.6	6.56	16.2	2.33	11.8

Table A3. Cont.

Sample	Sc	V	Cr	Co	Ni	Rb	Sr	Y	Zr	Nb	Ba	La	Ce	Pr	Nd
AC17-08	39.3	332	96.8	66.8	162	27.6	145	27	74.4	5.36	111	6.39	15.3	2.09	11.3
P-31b	-	370	35.2	45.4	51.9	43.8	244	21.1	87.5	11.9	199	11.5	27.8	3.6	14.2
P-32a	-	431	75.1	51.9	69.8	8.13	190	28.5	86.5	5.72	65.6	5.82	16.2	2.51	11.8
P-31e	37.3	384	78.8	48.3	65.9	19.1	188	24.9	67.4	4.04	141	3.59	9.57	1.55	7.88
325b	38.7	464	98.4	55.1	55	18.6	148	36.3	106	7.68	125	8.98	21.7	3.05	14.4
AC17-05	42.5	541	73.6	64.6	88	6.41	218	32.1	110	6.8	45.7	5.92	14.6	2.62	14
P-29a	-	374	116	51	79.5	10.7	161	23.8	40	3.36	98.4	3.37	9.25	1.58	7.99
P-30	-	425	104	60.3	80.8	10.9	140	29.5	77.7	5.66	103	5.47	13.9	2.17	10.3
AC17-03	48.6	380	61.8	47.7	59.9	5.49	128	24.3	62.5	3.21	23.5	3.21	8.17	1.37	7.64
AC17-04	50.9	338	431	55.1	139	16.9	165	19.3	49.9	2.32	114	2.16	6.87	1.05	5.47
AS18-21	33.5	418	20.4	40.1	45.7	48	481	24.6	69.9	3.49	1760	4.51	11.2	1.59	8.01
AS18-22	31	427	145	39.4	73.4	30	167	21.5	58.7	2.69	1160	3.03	8.32	1.31	7.23
AC17-16*	41.4	292	192	46.1	76.8	34.1	645	21.5	64	2.78	1360	3.41	9.17	1.51	7.47
AC17-17	46.1	399	213	51.3	101	9.56	180	27.4	83.5	3.92	71.8	3.98	11.6	1.95	10.1
AS18-19	49.5	433	98.9	51.2	68.4	20	130	29.3	76.7	5.24	137	3.99	10.5	1.78	9.07
SM17-16	49.7	408	112	54.3	74.5	25	112	26.3	66.3	3.42	48.1	3.21	8.61	1.35	6.79
LOD	0.2	2.5	1.0	0.5	1.0	2	1	0.1	0.5	0.5	3	0.01	0.01	0.01	0.01

Compositions determined by ICP-MS using an ELAN 6100 DRC ICP-MS instrument. All values are given in ppm.

Table A4. The results of whole-Rock Major and Trace Element Measurements (continuation).

Sample	Sm	Eu	Gd	Tb	Dy	Ho	Er	Tm	Yb	Lu	Hf	Ta	Pb	Th	U
AC17-22	9.57	2.55	8.68	1.35	9.3	1.85	5.78	0.83	5.41	0.66	6.97	1.95	3.09	2.89	0.89
AC17-23	5.03	1.52	5.97	0.99	7.73	1.73	4.51	0.72	4.41	0.56	3.35	0.53	1.94	1.75	0.51
L16-36	9.43	3.18	11.4	2.04	13.2	2.67	7.77	1.19	7.46	1.18	7.13	1.27	4.16	3.75	0.97
200/11	4.55	1.54	5.33	0.97	6.78	1.42	4.13	0.65	3.76	0.62	3.37	0.56	37.7	1.7	0.52
325	4.31	1.43	5.03	0.96	6.19	1.44	4.01	0.65	3.62	0.57	3.77	0.61	122	2	0.56
AC17-01	6.36	1.66	7.43	1.13	7.9	1.73	5.22	0.69	5.48	0.62	5.14	0.95	5.5	4.66	1.3
AC17-02	6.44	1.81	7.72	1.16	7.61	1.67	4.75	0.71	4.72	0.61	5.09	0.94	5.69	4.47	1.12
AC17-06	4.42	1.35	5.13	0.94	5.71	1.26	3.96	0.57	3.9	0.44	3.17	0.48	2.28	1.7	0.54
AC17-10	6.8	1.73	7.84	1.36	8.84	2.04	5.89	0.94	6.11	0.74	5.14	0.81	2.82	3.16	0.92
P-25	3.84	1.33	5.33	0.904	5.19	1.2	3.27	0.479	2.66	0.456	2.78	0.4	-	0.83	0.33
L16-103	4.76	1.82	6.26	1.08	7.14	1.5	4.3	0.64	4.12	0.65	3.58	0.62	-	1.89	0.48
P-26a	4.3	1.31	4.74	0.91	6.32	1.23	4.01	0.56	4	0.47	3.06	0.5	-	2.04	1.43
L16-105	6.29	2.01	7.48	1.25	7.78	1.66	4.58	0.67	4.33	0.67	4.74	1.07	4.43	3.86	0.97
P-27v	3.84	1.25	4.07	0.81	5.44	1.21	3.46	0.47	3.07	0.49	3.09	0.54	4.72	0.74	0.32
AC17-07	3.23	1.15	4.18	0.64	4.79	1.14	2.95	0.49	3.13	0.39	2.39	0.39	2.06	1.37	0.31
AC17-08	3.48	1.13	3.78	0.67	4.5	1.12	2.76	0.46	3	0.33	2.21	0.36	2.27	1.22	0.34
P-31b	3.53	1.05	3.18	0.62	3.88	0.79	2.54	0.31	2.3	0.39	2.15	0.94	-	2.02	2.84
P-32a	3.83	1.31	4.27	0.81	5.5	1.04	3.12	0.47	3.04	0.44	2.98	0.43	-	1.09	0.64
P-31e	2.54	0.89	2.96	0.66	3.91	0.98	2.55	0.44	2.27	0.39	2.17	0.27	1.58	0.39	0.21
325b	3.74	1.38	4.74	1.01	6.22	1.48	3.9	0.58	3.69	0.49	3.45	0.49	30	1.33	0.49
AC17-05	4.43	1.49	5.12	0.79	5.06	1.22	3.57	0.53	3.55	0.43	3.27	0.48	1.63	0.62	0.25
P-29a	2.85	1.02	3.22	0.57	4.43	0.92	2.83	0.39	2.81	0.32	1.96	0.19	-	0.26	0.1
P-30	3.39	1.21	3.92	0.77	5.38	1.18	3.43	0.5	3.1	0.44	2.56	0.31	-	1.28	6.12
AC17-03	2.45	0.87	3.21	0.59	4.33	0.94	2.69	0.44	3.02	0.35	1.7	0.19	1	0.27	0.12
AC17-04	2.21	0.76	2.79	0.47	3.19	0.68	1.97	0.33	2.12	0.27	1.31	0.17	1.16	0.22	0.1
AS18-21	2.86	0.99	3.52	0.63	4.1	0.88	2.66	0.41	2.74	0.39	1.98	0.24	-	0.68	0.18
AS18-22	2.52	0.98	3.57	0.58	3.82	0.83	2.35	0.34	2.21	0.33	1.65	0.19	-	0.24	0.1
AC17-16*	2.5	1.18	3.18	0.44	3.56	0.81	2.11	0.33	2.05	0.27	1.91	0.2	2.68	0.55	0.21
AC17-17	3.47	1.19	4.24	0.71	4.75	1.1	2.91	0.4	2.6	0.4	2.44	0.36	-	0.4	0.12
AS18-19	3.33	1.28	3.95	0.65	4.76	1.18	3.05	0.52	2.96	0.48	2.25	0.57	-	0.32	0.11
SM17-16	2.33	0.92	3.39	0.64	4.38	0.95	3	0.38	3.13	0.36	1.84	0.18	2.69	0.32	0.12
LOD	0.005	0.005	0.01	0.005	0.01	0.005	0.01	0.005	0.01	0.005	0.01	0.1	1.0	0.1	0.1

Compositions determined by ICP-MS using an ELAN 6100 DRC ICP-MS instrument. All values are given in ppm.

References

1. Parfenov, L.M.; Prokopiev, A.V.; Gaiduk, V.V. Cretaceous frontal thrusts of the Verkhoyansk fold belt, eastern Siberia. *Tectonics* **1995**, *14*, 342–358. [\[CrossRef\]](#)
2. Prokojev, A.V.; Deikunenko, A.V. Deformational Structures of the Fold-Thrust Belts. In *Tectonics, Geodynamics and Metallogeny of the Territory of the Republic of Sakha (Yakutia)*; Parfenov, L.M., Kuzmin, M.I., Eds.; MAIK Science/Interperiodika: Moscow, Russia, 2001; pp. 156–198. ISBN 578460046X.
3. Khudoley, A.K.; Rainbird, R.H.; Stern, R.A.; Kropachev, A.P.; Heaman, L.M.; Zanin, A.M.; Podkovyrov, V.N.; Belova, V.N.; Sukhorukov, V.I. Sedimentary evolution of the Riphean-Vendian basin of southeastern Siberia. *Precamb. Res.* **2001**, *111*, 129–163. [\[CrossRef\]](#)
4. Khudoley, A.K.; Prokopiev, A.V. Defining the Eastern Boundary of the North Asian Craton from Structural and Subsidence History Studies of the Verkhoyansk Fold-and-Thrust Belt. In *Whence the Mountains? Inquiries into the Evolution of Orogenic Systems: A Volume in Honor of Raymond A. Price*; Sears, J.W., Harms, T.A., Evenchick, C.A., Eds.; Geological Society of America: Boulder, CO, USA, 2007; Volume 433, pp. 391–410. ISBN 9780813724331.
5. Kiselev, A.I.; Ernst, R.E.; Yarmolyuk, V.V.; Egorov, K.N. Radiating rifts and dyke swarms of the middle Paleozoic Yakutsk plume of eastern Siberian craton. *J. Asian Earth Sci.* **2012**, *45*, 1–16. [\[CrossRef\]](#)
6. Khudoley, A.K.; Kropachev, A.P.; Tkachenko, V.I.; Rublev, A.G.; Sergeev, S.A.; Matukov, D.I.; Lyahnitskaya, O.Y. Mesoproterozoic to Neoproterozoic Evolution of the Siberian Craton and Adjacent Microcontinents: An Overview with Constraints for a Laurentian Connection. In *Proterozoic Geology of Western North America and Siberia*; Society for Sedimentary Geology: Tulsa, OK, USA, 2007; pp. 209–226.
7. Khudoley, A.K.; Prokopiev, A.V.; Chamberlain, K.R.; Ernst, R.E.; Jowitt, S.M.; Malyshev, S.V.; Zaitsev, A.I.; Kropachev, A.P.; Koroleva, O.V. Early Paleozoic mafic magmatic events on the eastern margin of the Siberian Craton. *Lithos* **2013**, *174*, 44–56. [\[CrossRef\]](#)
8. Ernst, R.E. Large Igneous Provinces. In *Large Igneous Provinces*; Ernst, R.E., Ed.; Cambridge University Press: Cambridge, UK, 2014; p. 653. ISBN 9780521871778.
9. Yan-Zhin-Shin, V.A. *Tectonics of the Sette-Daban Horst-Anticlinorium*; JFSO Academy of Sciences of the USSR: Yakutsk, Russia, 1983.
10. Rainbird, R.H.; Stern, R.A.; Khudoley, A.K.; Kropachev, A.P.; Heaman, L.M.; Sukhorukov, V.I. U-Pb geochronology of Riphean sandstone and gabbro from southeast Siberia and its bearing on the Laurentia-Siberia connection. *Earth Planet. Sci. Lett.* **1998**, *164*, 409–420. [\[CrossRef\]](#)
11. Pavlov, V.E.; Gallet, Y.; Petrov, P.Y.; Zhuravlev, D.Z.; Shatsillo, A.V. The Ui Group and Late Riphean Sills in the Uchur-Maya Area: Isotope and Paleomagnetic Data and the Problem of the Rodinia Supercontinent. *Geotectonics* **2002**, *36*, 278–292.
12. Starnikov, A.I. *Geological Map of the USSR, Scale 1:200000, Sheet P-53-XXXV*; VSEGEI: Saint Petersburg, Russia, 1983.
13. Semikhatov, M.A.; Serebryakov, S.N. *Siberian Hypostratotype of Riphean*; Nauka: Moscow, Russia, 1983.
14. Sukhorukov, V.I. The Upper Riphean Type Sections of the Ulakhan-Bam Ridge. In *Late Precambrian and Early Paleozoic of Siberia. Siberian Platform and Outer Part of the Altai-Sayan Fold Belt*; Khomentovskiy, V.V., Ed.; IGG Press: Novosibirsk, Russia, 1986; pp. 23–64.
15. Khudoley, A.K.; Guriev, G.A. Influence of syn-sedimentary faults on orogenic structure: Examples from the Neoproterozoic–Mesozoic east Siberian passive margin. *Tectonophysics* **2003**, *365*, 23–43. [\[CrossRef\]](#)
16. Shenfil, V.Y. *Upper Precambrian of the Siberian Platform*; Nauka: Novosibirsk, Russia, 1991.
17. Kuznetsov, A.B.; Kaurova, O.K.; Petrov, P.Y. Pb–Pb Isochron age and Sr-isotopic signature of the Upper Yudoma carbonate sediments (the vendian of the Yudoma-Maya trough, Eastern Siberia). *Dokl. Earth Sci.* **2003**, *393*, 1093–1097.
18. Khudoley, A.; Chamberlain, K.; Ershova, V.; Sears, J.; Prokopiev, A.; MacLean, J.; Kazakova, G.; Malyshev, S.; Molchanov, A.; Kullerud, K.; et al. Proterozoic supercontinental restorations: Constraints from provenance studies of Mesoproterozoic to Cambrian clastic rocks, eastern Siberian Craton. *Precamb. Res.* **2015**, *259*, 78–94. [\[CrossRef\]](#)
19. Malyshev, S.V.; Khudoley, A.K.; Prokopiev, A.V.; Ershova, V.B.; Kazakova, G.G.; Terentyeva, L.B. Source rocks of Carboniferous–Lower Cretaceous terrigenous sediments of the northeastern Siberian Platform: Results of Sm–Nd isotope-geochemical studies. *Russ. Geol. Geophys.* **2016**, *57*, 421–433. [\[CrossRef\]](#)

20. Jacobsen, S.B.; Wasserburg, G.J. Sm-Nd isotopic evolution of chondrites and achondrites, II. *Earth Planet. Sci. Lett.* **1984**, *67*, 137–150. [[CrossRef](#)]
21. Bayanova, T.B. *Age of Reference Geological Complexes of the Kola Peninsula and Duration of the Magmatic Processes*; Nauka: Saint Petersburg, Russia, 2004.
22. Le Bas, M.J.; Le Maitre, R.W.; Streckeisen, A.; Zanettin, B. A Chemical Classification of Volcanic Rocks Based on the Total Alkali-Silica Diagram. *J. Petrol.* **1986**, *27*, 745–750. [[CrossRef](#)]
23. Kuno, H. Differentiation of Basalt Magmas. In *Basalts: The Poldervaart Treatise on Rock of Basaltic Composition*; Hess, H.H., Poldervaart, A., Eds.; Interscience: New York, NY, USA, 1968; Volume 2, pp. 632–688.
24. Pearce, J.A.; Stern, R.J.; Bloomer, S.H.; Fryer, P. Geochemical mapping of the Mariana arc-basin system: Implications for the nature and distribution of subduction components. *Geochem. Geophys. Geosyst.* **2005**, *6*, 1–27. [[CrossRef](#)]
25. Babechuk, M.G.; Kamber, B.S. An estimate of 1.9 Ga mantle depletion using the high-field-strength elements and Nd–Pb isotopes of ocean floor basalts, Flin Flon Belt, Canada. *Precamb. Res.* **2011**, *189*, 114–139. [[CrossRef](#)]
26. Sun, S.; McDonough, W. Chemical and Isotopic Systematics of Ocean Basalts: Implications for Mantle Composition and Processes. In *Magmatism in the Ocean Basins*; Geological Society Publishing: Bath, UK, 1989; Volume 42, pp. 313–345.
27. Gale, A.; Dalton, C.A.; Langmuir, C.H.; Su, Y.; Schilling, J.G. The mean composition of ocean ridge basalts. *Geochem. Geophys. Geosyst.* **2013**, *14*, 489–518. [[CrossRef](#)]
28. Kogiso, T.; Tatsumi, Y.; Nakano, S. Trace element transport during dehydration processes in the subducted oceanic crust: 1. Experiments and implications for the origin of ocean island basalts. *Earth Planet. Sci. Lett.* **1997**, *148*, 193–205. [[CrossRef](#)]
29. Turner, S.; Caulfield, J.; Turner, M.; van Keken, P.; Maury, R.; Sandiford, M.; Prouteau, G. Recent contribution of sediments and fluids to the mantle’s volatile budget. *Nat. Geosci.* **2012**, *5*, 50–54. [[CrossRef](#)]
30. Zhang, B.; Yoshino, T.; Yamazaki, D.; Manthilake, G.; Katsura, T. Electrical conductivity anisotropy in partially molten peridotite under shear deformation. *Earth Planet. Sci. Lett.* **2014**, *405*, 98–109. [[CrossRef](#)]
31. Stracke, A.; Bizimis, M.; Salters, V.J.M. Recycling oceanic crust: Quantitative constraints. *Geochem. Geophys. Geosyst.* **2003**, *4*. [[CrossRef](#)]
32. Class, C.; Miller, D.M.; Goldstein, S.L.; Langmuir, C.H. Distinguishing melt and fluid subduction components in Umnak Volcanics, Aleutian Arc. *Geochem. Geophys. Geosyst.* **2000**, *1*, 1–28. [[CrossRef](#)]
33. Johnson, M.C.; Plank, T. Dehydration and melting experiments constrain the fate of subducted sediments. *Geochem. Geophys. Geosyst.* **2000**, *1*. [[CrossRef](#)]
34. Pearce, J.; Peate, D. Tectonic Implications of the Composition of Volcanic ARC Magmas. *Annu. Rev. Earth Planet. Sci.* **1995**, *23*, 251–285. [[CrossRef](#)]
35. Pearce, J.A. Geochemical fingerprinting of oceanic basalts with applications to ophiolite classification and the search for Archean oceanic crust. *Lithos* **2008**, *100*, 14–48. [[CrossRef](#)]
36. Ivanov, A.V.; Demonerova, E.I.; Rasskazov, S.V.; Yasnygina, T.A. Low-Ti melts from the southeastern Siberian Traps Large Igneous Province: Evidence for a water-rich mantle source? *J. Earth Syst. Sci.* **2008**, *117*. [[CrossRef](#)]
37. Jourdan, F.; Bertrand, H.; Schärer, U.; Blichert-Toft, J.; Féraud, G.; Kampunzu, A.B. Major and trace element and Sr, Nd, Hf, and Pb isotope compositions of the Karoo large igneous province, Botswana-Zimbabwe: Lithosphere vs Mantle Plume Contribution. *J. Petrol.* **2007**, *48*, 1043–1077. [[CrossRef](#)]
38. Condie, K.C. High field strength element ratios in Archean basalts: A window to evolving sources of mantle plumes? *Lithos* **2005**, *79*, 491–504. [[CrossRef](#)]
39. Condie, K.C. Incompatible element ratios in oceanic basalts and komatiites: Tracking deep mantle sources and continental growth rates with time. *Geochem. Geophys. Geosyst.* **2003**, *4*, 1–28. [[CrossRef](#)]
40. Weaver, B.L. The origin of ocean island basalt end-member compositions: Trace element and isotopic constraints. *Earth Planet. Sci. Lett.* **1991**, *104*, 381–397. [[CrossRef](#)]
41. Smith, P.M.; Asimow, P.D. Adibat-1ph: A new public front-end to the MELTS, pMELTS, and pHMELTS models. *Geochem. Geophys. Geosyst.* **2005**, *6*, 1–8. [[CrossRef](#)]
42. Bédard, J. A catalytic delamination-driven model for coupled genesis of Archean crust and sub-continental lithospheric mantle. *Geochim. Cosmochim. Acta* **2006**, *70*, 1188–1214. [[CrossRef](#)]
43. Salters, V.J.M.; Stracke, A. Composition of the depleted mantle. *Geochem. Geophys. Geosyst.* **2004**, *5*. [[CrossRef](#)]

44. Palme, H.; O'Neill, H.S.C. Cosmochemical Estimates of Mantle Composition. In *Treatise on Geochemistry*; Holland, H.D., Turekian, K.K., Eds.; Elsevier: Amsterdam, The Netherlands, 2003; pp. 1–38. ISBN 978-0-08-043751-4.
45. Taylor, S.R.; McLennan, S.M. The geochemical evolution of the continental crust. *Rev. Geophys.* **1995**, *33*, 241–265. [[CrossRef](#)]
46. PetDB Database. Available online: www.earthchem.org/petdb (accessed on 15 April 2020).
47. Evans, D.A.D.; Mitchell, R.N. Assembly and breakup of the core of Paleoproterozoic–Mesoproterozoic supercontinent Nuna. *Geology* **2011**, *39*, 443–446. [[CrossRef](#)]
48. Spencer, C.J.; Cawood, P.A.; Hawkesworth, C.J.; Prave, A.R.; Roberts, N.M.W.; Horstwood, M.S.A.; Whitehouse, M.J. EIMF Generation and preservation of continental crust in the Grenville Orogeny. *Geosci. Front.* **2015**, *6*, 357–372. [[CrossRef](#)]
49. Pavlov, V.E.; Shatsillo, A.V.; Petrov, P.Y. Paleomagnetism of the upper Riphean deposits in the Turukhansk and Olenek uplifts and Uda Pre-Sayan region and the neoproterozoic drift of the Siberian Platform. *Izv. Phys. Solid Earth* **2015**, *51*, 716–747. [[CrossRef](#)]
50. Sheldrick, T.C.; Barry, T.L.; Van Hinsbergen, D.J.J.; Kempton, P.D. Constraining lithospheric removal and asthenospheric input to melts in Central Asia: A geochemical study of Triassic to Cretaceous magmatic rocks in the Gobi Altai (Mongolia). *Lithos* **2018**, *296*, 297–315. [[CrossRef](#)]
51. Ou, Q.; Wang, Q.; Wyman, D.A.; Zhang, C.; Hao, L.-L.; Dan, W.; Jiang, Z.-Q.; Wu, F.-Y.; Yang, J.-H.; Zhang, H.-X.; et al. Postcollisional delamination and partial melting of enriched lithospheric mantle: Evidence from Oligocene (ca. 30 Ma) potassium-rich lavas in the Gemuchaka area of the central Qiangtang Block, Tibet. *GSA Bull.* **2018**, *131*, 1385–1408. [[CrossRef](#)]
52. Ivanov, A.V. Why Volatiles are Required for Craton. In *The Interdisciplinary Earth: A Volume in Honor of Don L. Anderson*; Foulger, G.R., Lustrino, M., King, S.D., Eds.; Geological Society of America: Boulder, CO, USA, 2015; Volume 514, pp. 325–338. ISBN 9780813725147.
53. Pisarevsky, S.A.; Elming, S.-Å.; Pesonen, L.J.; Li, Z.-X. Mesoproterozoic paleogeography: Supercontinent and beyond. *Precamb. Res.* **2014**, *244*, 207–225. [[CrossRef](#)]



© 2020 by the authors. Licensee MDPI, Basel, Switzerland. This article is an open access article distributed under the terms and conditions of the Creative Commons Attribution (CC BY) license (<http://creativecommons.org/licenses/by/4.0/>).